
Numerical Study of the Dewing Phenomenon on Vehicular Window Glass

Yang Yue^{1,3}, Yuqi Huang^{1*}, Jisheng Zhao²

1. Department of Energy Engineering, Zhejiang University, Hangzhou 310027
2. Fluids Laboratory for Aeronautical and Industrial Research, Department of Mechanical and Aerospace Engineering, Monash University, Clayton, VIC 3800, Australia
3. Department of Mechanical Engineering and Applied Mechanics, University of Pennsylvania, Philadelphia, PA 19104, USA

Abstract

The problem of vehicle window dewing not only affects the occupants' comfort in the vehicle, interferes with the driver's sight, but also potentially threatens the safety of driving as well as electronic equipment in the vehicle. Therefore, analyzing the condensation process inside the cabin is of great practical concern to improve driving comfort and safety. This study is focused on the process of condensation and defogging in the cabin of a truck model, where the outside heat dissipation and internal air conditioning system are considered together. The condensation process simulation based on the EWF (Eulerian Wall Film) model of ANSYS Fluent in conjunction with user defined functions was validated by comparing with experiments. Then, the flow domain around a simplified three-dimensional truck model was established to conduct the external thermal conditions. By examining various conditions of the air inlet mode, temperature, humidity and speeds of the ventilation system, it was found that the mass flow rate, inlet temperature and humidity could influence the dewing film thickness directly. Of significance, when the air conditioning system was taken as the main defogging approach, with the relative humidity set at approximately 20% and the temperature above 320K, the dewing phenomenon was eliminated at the highest efficiency. These results would be useful to provide suggestions for the future design of automotive air conditioning systems.

Keywords: vehicle window dewing; phase change; condensation; defog; air conditioning

1. Introduction

Dewing is a very common phenomenon as it refers to vapor condensing on the surface of an object when the temperature is lower than a critical (dewing) point. In engineering applications, it can potentially cause severe hazards. For example, dewing in pipes and equipment will accelerate corrosion process and reduce the component life; bacteria in human nasal cavity can reproduce rapidly in dews, causing respiratory diseases[1]. Similar to human beings, vehicles are also severely affected by dewing problem in the cabin. Dews on the vehicle windows would not only influence the sight of the driver, potentially leading to a traffic accident, but also increase the humidity inside the vehicle, affecting the comfort of occupants. With the increasing number and complexity of electronic devices in vehicles, which are sensitive to the humidity and temperature, the vehicular control system can also be affected by dewing problem.

To deal with the dewing problem, three primary methods have often been used: changing the ventilation condition, raising the window surface temperature and using anti-fogging materials. However, the latter two have considerable drawbacks; for example, the technique of adding the heating wire in the glass to raise window surface temperature may not be applied in the front window for the reason of blocking eyesight. Anti-fogging materials, such as anti-clouding agent and soapy water, could reduce the surface tension of water to promote membrane condensation, but the effective time duration of this approach is very short and it may also increase the humidity inside the vehicle. Thus, controlling the air conditioning system appears to be the most widely used method of defogging, despite energy consumption. It is of interest to investigate various operating conditions of a ventilating system to efficiently diminish the dew phenomenon .

While a large amount of work on dewing phenomenon has been focused on buildings [2][3], nuclear services [4][5], and heat transfer pipe systems [6][7], much less research attention has been paid to the dewing problem on vehicle windows. Previous studies have shown that CFD (Computational Fluid Dynamics) method is a validated approach in analyzing the airflow conditions and water vapor condensation progress in various circumstances [8]-[10]. At the end of last century, Hara and Fujitani [11]-[12] conducted a series of two- and three-dimensional (2-D and 3-D) simulations on the airflow and temperature field inside a car cabin, showing that numerical simulations could perfectly reflect the heat transfer and flow process. Through numerical simulations,

Van der Kooi [13] analyzed the airflow field and temperature distribution inside a vehicle cabin with different inlet positions, and reported best solutions for the optimal indoor climate based on the temperature and contamination, as well as the condensation results. J. Currel [14] also numerically analyzed the flow field in a vehicle cabin to optimize the thermal comfort for passengers with the consideration of thermophysiological model for the passengers and radiation. AbdulNour et al. [15][16] and Aroussi et al. [17]-[19] conducted both experiments and numerical simulations to investigate the defrosting and demisting performance, but with little attend given to the dewing process. Recently, Arman Dwiarton [20] numerically investigated the defogging characteristics of vehicle windows. In their numerical simulations, the fog layer attached to the glass surface was considered as a liquid film of the same thickness, and two models were used: on model for analyzing one-dimensional unsteady heat transfer, and the other for simulating the evaporation characteristics of the liquid film. Kharat and Nandgaokar [21] simulated the internal heat environment of a vehicle model, and analyzed the mechanism of fogging and defogging on the window surfaces. They showed that numerical simulation results agreed well with experimental measurements. More recently, Liu et al. [28] conducted both experiments and numerical simulations to analyze the influence of external flow velocity, temperature and relative humidity on the return air utilization for electric vehicles. However, the above cited studies were mainly focused on the phase transform on the front windshield, neglecting the side and rear windows, where the distribution of humidity and temperature field in the cabin was not considered, and the influence of external flow fields was also ignored.

In summary, although there has been a considerable amount of studies conducted on the flow field and the heat environment inside vehicle cabins, there is still a lack of the information of relationships between the external flow and the heat dissipation and condensation of vehicle windows. Thus, the present work aims to explore the mechanism of vehicle window dewing process under different air conditioning conditions via numerical simulations, to analyze the difference of dewing process under different air conditioning conditions, and to obtain the optimal operating state with a combination of ride comfort and energy consumption efficiency.

The study proceeds by describing the numerical methods in section 2. The results and discussion are presented in section 3. Finally, conclusions are drawn in section 4.

2. Methodology

2.1 Numerical simulation details

In this study, the numerical simulations were conducted using the commercial software ANSYS FLUENT 17.0 combined with user defined functions (UDFs) as the main solver. It should be note that the k- ϵ Standard model was selected as the turbulence model, and Eulerian Wall Film (EWF) was chosen as the multiphase model. Assuming that the thickness of the liquid film was less than the radius of the wall curvature, the properties of the liquid film in the thickness direction were certain and sufficiently thin to be regarded as the two squares parallel to the wall flow. Accordingly, the basic control equations are as follows [22]:

Mass conservation equation:

$$\frac{\partial h}{\partial t} + \nabla_s [h\bar{V}_l] = \frac{\dot{m}_s}{\rho_l} \quad (1)$$

where ρ_l is the liquid density, h is the film height, ∇_s is the surface gradient operator, \bar{V}_l the mean film velocity and \dot{m}_s is the mass source per unit wall area due to droplet collection, film separation, film stripping, and phase change.

Momentum conservation equation:

$$\frac{\partial h\bar{V}_l}{\partial t} + \nabla_s (h\bar{V}_l\bar{V}_l) = -\frac{h\nabla_s P_L}{\rho_l} + (\bar{g}_\tau)h + \frac{3}{2\rho_l}\bar{\tau}_{fs} - \frac{3}{2\rho_l}\bar{V}_l + \frac{\dot{q}}{\rho_l} \quad (2)$$

In which,

$$P_L = P_{gas} + P_h + P_\sigma$$

$$P_h = -\rho h(\bar{n} \cdot \bar{g})$$

$$P_\sigma = -\sigma\nabla_s(\nabla_s h)$$

The left hand of equation (2) represent transient and convection effects. On the right hand side, the first term includes the effects of gas-flow pressure, the gravity component normal to the wall surface (known as spreading), and surface tension; the second term represents the effect of gravity in the direction parallel to the film; the third term is the viscous shear force at the gas-film interface; the fourth term represents the viscous force in the film, and the last term is associated with droplet collection or separation. Note that in arriving at the shear and viscous terms on the RHS, a parabolic

film velocity profile has been assumed.

Energy conservation equation:

$$\frac{\partial h \vec{V}_l}{\partial t} + \nabla_s (\vec{V}_f h T_f) = \frac{1}{\rho C_p} \left\{ 2k_f \left[\frac{T_s + T_w}{h} - \frac{2T_f}{h} \right] + \dot{q}_{imp} + \dot{m}_{vap} L(T_s) \right\} \quad (3)$$

where, T_s is temperature at the film-gas interface, T_f is the average film temperature and it is the dependent variable of the above equation, T_w is the wall temperature. \dot{q}_{imp} is the source term due to liquid impingement from the bulk flow to the wall. \dot{m}_{vap} is the mass vaporization or condensation rate and L is the latent heat associated with the phase change.

In order to analyze the transient process of condensation, UDFs were applied in the present simulations. The water vapor mass fraction is determined by [23]:

$$d = \frac{m_v}{m_a} = \frac{M_v p_v}{M_a p_a} = 0.622 \varphi \frac{p_v}{p - p_v} \quad (4)$$

$$\omega = \frac{d}{1+d} \quad (5)$$

Thus, the water vapor diffusion coefficient is given by

$$C_{diff} = \frac{0.926 \times 10^{-6}}{0.001P} \cdot \frac{T_{cell}^{2.5}}{T_{cell} + 245} \quad (6)$$

Saturated pressure of water vapor at a certain temperature:

$$P_s = \begin{cases} 49.31T' + 611.45 \\ T'(T'(T'(T'(T'(c5) + c4) + c3) + c2) + c1) + \\ c0 + i(i(i(i(n4) + n3) + n2) + n1) \\ (T' = T - 273.15, i = \frac{1}{T' + 0.001}) \end{cases} \quad (7)$$

where d is the water vapor mass fraction and φ is the relative humidity; m_v , M_v , m_a , M_a , represent the mass\molar mass of vapor and air respectively; p_v , p_a , p are the pressure of the vapor, air, and total pressure.

2.2 Validation

To validate the numerical model and UDFs used in this study, the CONAN model used experimentally by Ambrosini [24] was adopted as the reference for condensation benchmark testing.

Figure 1 shows the key parameters of Ambrosini's experimental CONAN model, together with the present numerical finite element model (FEM). In the present FEM, the structured mesh was applied, and the near-wall grids were densified. The nodes number in three direction was $52 \times 52 \times$

120, and the total number of grids was 320,000. It should also be noted that part of the boundary conditions was adopted from the studies of Laidlaw Vyskocil's [25], where the CONAN model was also used as the validation reference. In the present test, the turbulence intensity of inlet was set at 2%; the hydraulic diameter was 0.003m; pressure of outlet was barometric pressure; the remaining walls were adiabatic; and the acceleration of gravity was 9.81m/s. Three different experimental inlet parameters were chosen to be simulated, as shown in table 1.

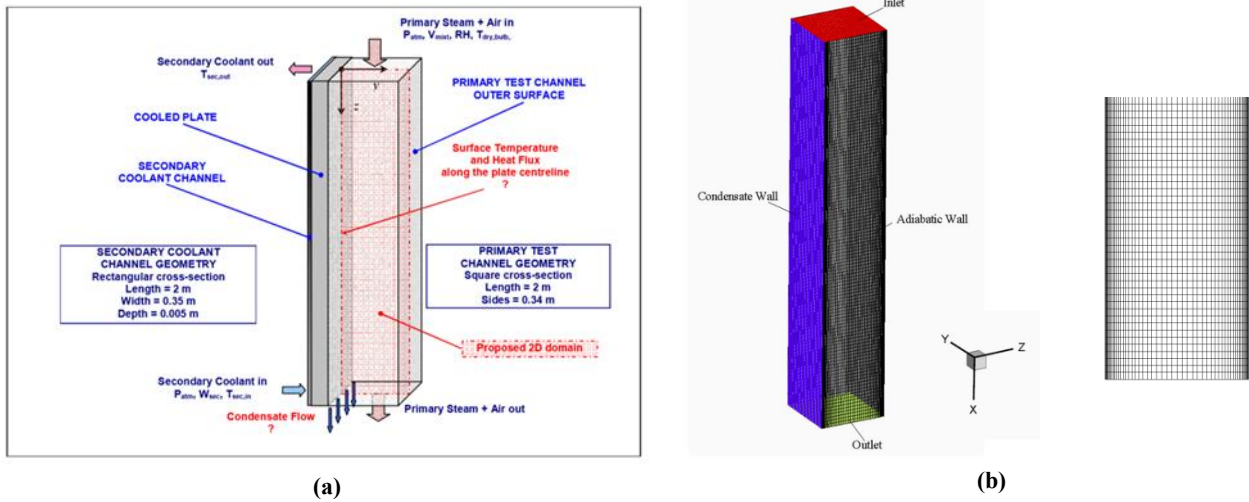


Figure 1: Schematics of (a) the experimental model used by Ambrosini [24] and (b) the finite element model and its near-wall grids. Note that the wet air flow moves from the top to the bottom through a square cross-sectional pipe, and it condenses on the cooled surfaces.

Table.1 Inlet Parameters of Validation Model

Cases	Inlet Parameters			
	V[m/s]	RH[%]	T[°C]	ω_{vap}
P30-T40-V25	2.63	100	97.5	0.8692
P20-T40-V25	2.59	100	89.5	0.5685
P10-T40-V25	2.58	100	79.8	0.3500

P - pressure; T - temperature; V - velocity; ω_{vap} - the mass fraction of water vapor.

Figure 2 shows contours of the mass fraction for three different fluids, namely liquid water, gaseous water and air, in the steady state. As can be seen, the liquid water concentrates on the lower part of the cooled plate due to the effect of gravity. The closer to the inlet, the water vapor mass fraction is resulted higher, and relative mass fraction of air and liquid water is smaller.

Furthermore, comparisons of the heat flux and temperature along the wall (in the X-direction) were made between the present simulations and the previous experiments of Ambrosini [24], as

shown in figures 3(a) and (b), respectively. It can be seen that the present results in general are in good agreement with the previous experimental measurements, showing the highly similar trends in both the heat flux and the temperature, which first decrease sharply with increases in the distance from the inlet prior to a stable gradually decreasing trend.

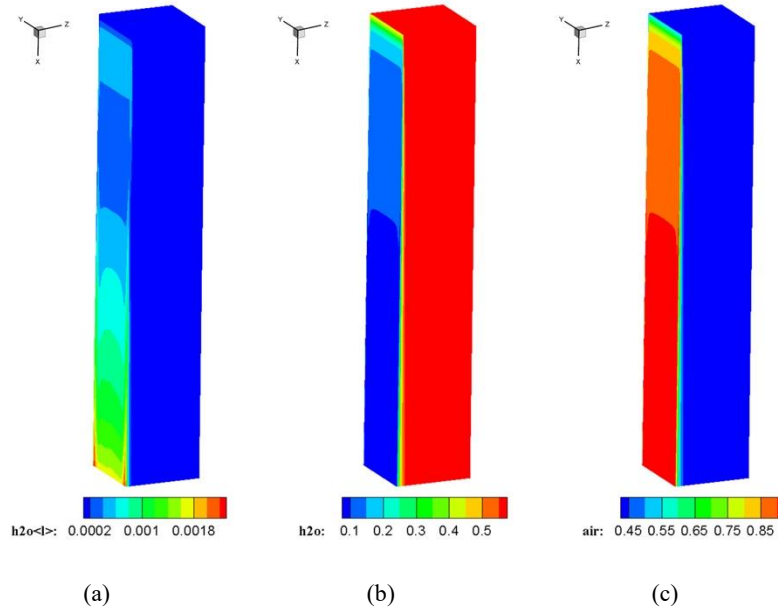


Figure 2: Distribution of the mass fraction (a) liquid water, (b) gaseous water and (c) air.

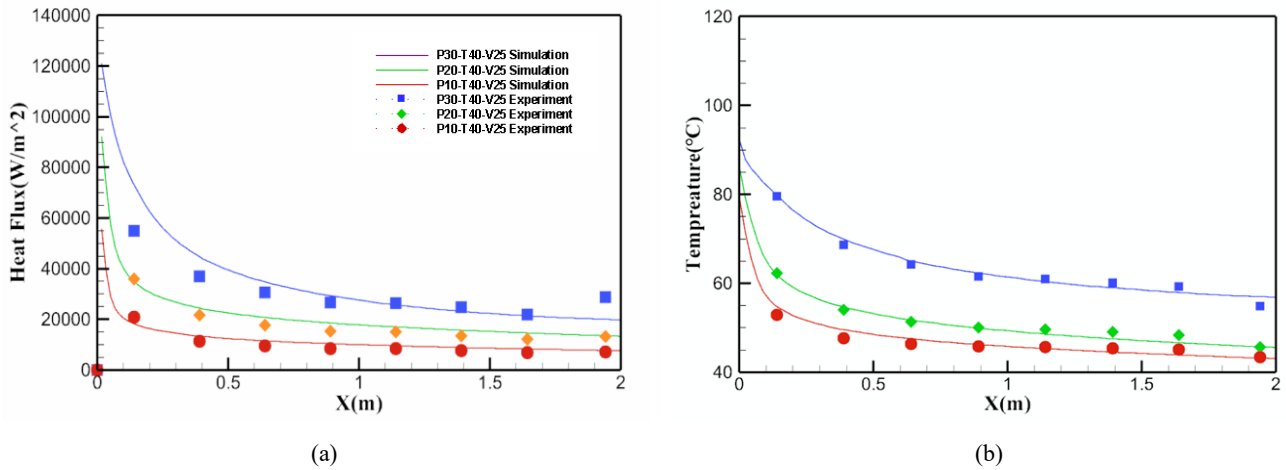


Figure 3 (a) Comparisons of the heat flux along the wall in the X-direction between the present numerical results and the previous experimental measurements by Ambrosini[24]. (b) Comparisons of the temperature along the wall in the X-direction between present numerical results and the previous experimental measurements by Ambrosini[24].

3. Discussions on truck model

Considering the complexity and difficulty of the modelling and limited computing resources, we focus here on a simplified truck cabin having relatively simple geometries. In this section, results

of the heat transfer coefficient of the vehicle windows and the condensation inside the cabin are presented together with the external and internal flow fields.

3.1 Geometric Parameters of Truck Model

The truck model used in this paper is based on the latest generation of DONGFENG, with appropriate simplifications, as shown in figure 4. The oversize of the truck head model is 1648 mm × 1800 mm × 1680 mm with four windows (two sides, one front and one rear). The sizes of the windows are shown in table 2.

Table.2 Geometric dimensions of the truck model windows.

Glass Position	Length [mm]	Width [mm]	Thickness [mm]	Area [mm ²]
Front	1500	800	5	1 210 000
Side	900	700	5	630 000
Back	1000	300	5	300 0

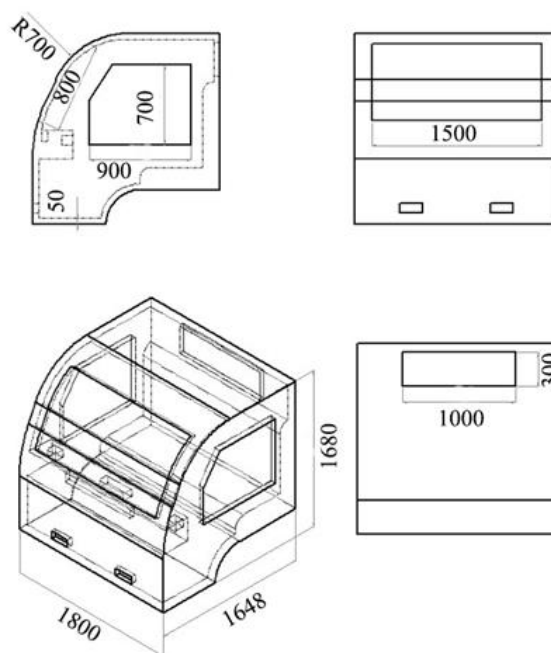


Figure. 4: Geometric dimensions of the truck model used in the present study

3.2 Simulation of External Flow Field

The flow around moving cars is a very complicated problem with profound flow velocity field, turbulence intensity and pressure distribution in different areas around the vehicle body. Thus, large

variations in the heat transfer coefficient of different windows may be induced, which can further influence the dewing process on the surface of the windows.

To simulate more accurately the heat transfer process on the vehicle windows, a trailer structure was added based on the original head model (see Yang et al [27]). The trailer and the truck head had the same dimensions: 4400 mm in length (L), 2000 mm in height (H) and 400mm in width (W) (the distance between the truck head). The computational domain ($4L \times 8W \times 8H$) was established by ANSYS ICEM, as shown in figure 5(a). The inlet was positioned $2L$ away from the front of the truck, while the outlet was $4L$ from the rear of the truck. This domain was large enough to eliminate the entrance effect. The unstructured tetrahedral mesh was applied and the grids near the truck body were densified, as shown in figure 5 (b). The total number of the grid elements was 1.86 million. The transient calculation was adopted in FLUENT. The time step was set to 0.2s, and total simulation time was 1000s with 20 iterations for each time step. The inlet flow velocity was set at 20m/s to simulate the drum of wheels in a real wind tunnel, and the temperature was 273K, noting that the walls and the ground were adiabatic. The temperature of the four windows was initially set at 283K. The window material was toughened glass (the physical parameters [26] are shown in table 3).

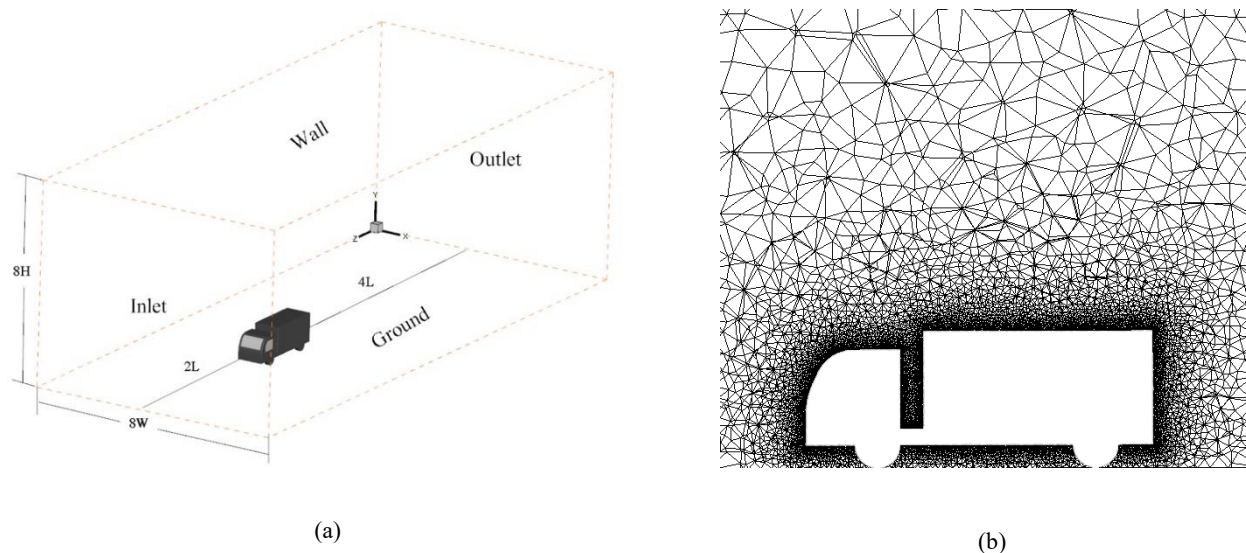


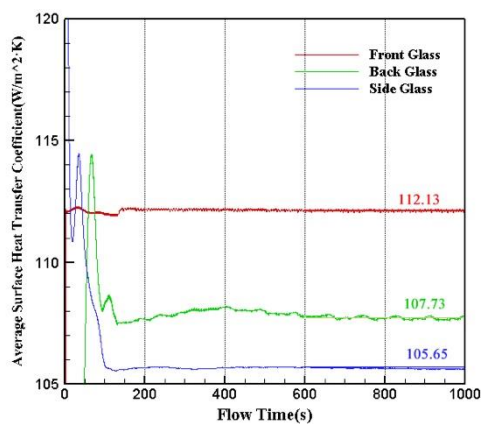
Figure 5: Scheme of the simulating model. (a) the computational domain for the external flow field and (b) grids in the Y-Z plane.

Table.3 Physical Parameters of toughened glass

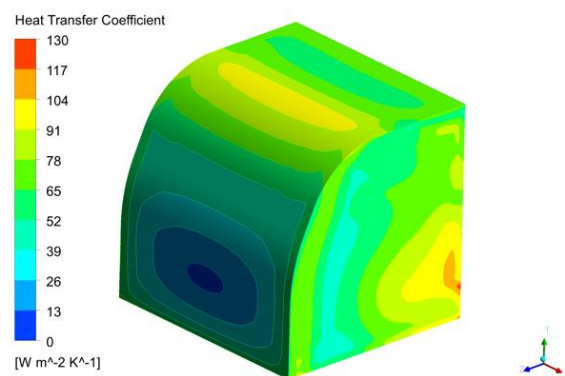
Material	Density[g/cm ³]	Specific Heat[j/kg·k]	Thermal Conductivity
Glass	2500	720	1.38

The surface-averaged heat transfer coefficient of the windows is shown in figure 6(a). As can be seen, the heat transfer coefficient in all cases become fairly stable after approximately 200s, where the differences between different windows are very small, with the highest value observed for the front window, followed by the side and back windows. It should be noted that the average heat transfer coefficients in the stable stage after 600s were chosen as in the boundary conditions for the simulations of condensation which will be presented.

Furthermore, figures 6(b), (c) and (d) show contours of the heat transfer coefficient and the pressure on the body surfaces, and the external flow velocity field, respectively. The minimum value of the heat transfer coefficient observed is in the lower part of the truck head where the heat transfer is directly impacted by the highest pressure and almost zero flow velocity. On the other hand, the highest heat transfer coefficient value occurs at the top of the truck head where the airflow displays the highest velocity and the flow separates. Moreover, the heat transfer coefficient of the front window, in general, is slightly higher than that of the side and rear windows. Therefore, it can be concluded that the heat transfer coefficient is strongly related to the local flow velocity and pressure distribution.



(a)



(b)

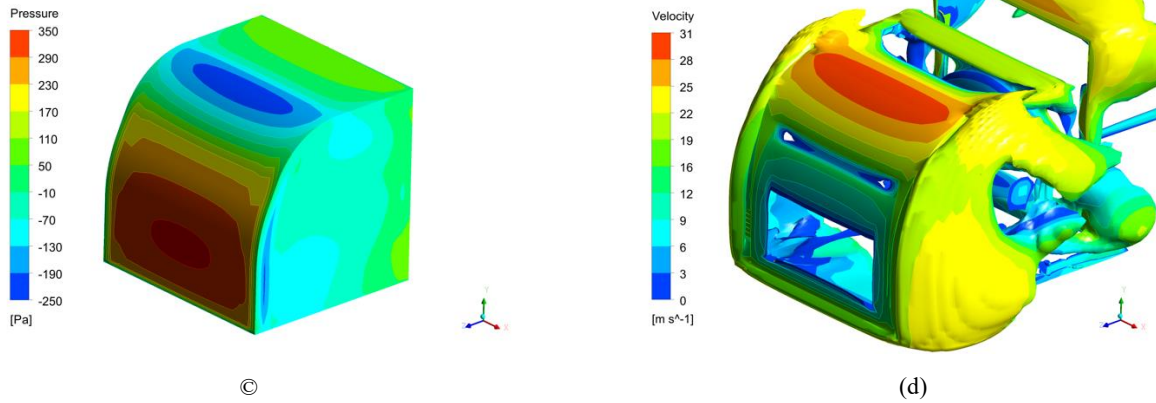


Figure 6: The heat and flow characters of the cabin. (a) the heat transfer coefficient of the cabin windows. (b) c contours of the heat transfer coefficient of the truck model. (c) the pressure distribution of the truck model. (d) contours of the external flow velocity field.

3.3 Dewing progress and analysis

3.3.1 Evaluation standard for the indoor thermal comfort

In addition to the dewing phenomenon, the thermal comfort of occupants in the vehicle is also of our concern in this article. The standard of indoor thermal comfort is based on ‘Code for Design of Heating Ventilation and Air Conditioning’ (GB50019-2003) shown in table 4.

Table.4 Evaluation standard for the indoor thermal comfort

Season	Temperature[K]	RH[%]	Velocity[m/s]
Summer	295-301	40-65	≤0.3
Winter	292-298	30-60	≤0.2

3.3.2 Computational domain

The computational domain used for the indoor thermal comfort study is shown in figure 7 (a). There are four inlets, including the main inlet (with a cross-sectional area of 960 mm²), two side inlet (with a cross-sectional area of 960 mm²), and a special defog inlet (with a cross-sectional area of 400 mm²) which is set below the front window. The two outlets (with a cross-sectional area of 160 mm²) are located below the control panel. The main inlet is located in the middle of the control panel and two smaller inlets are on each side of the cabin, while two outlets are located under the control panel, close to the driver’s feet position according to actual structure.

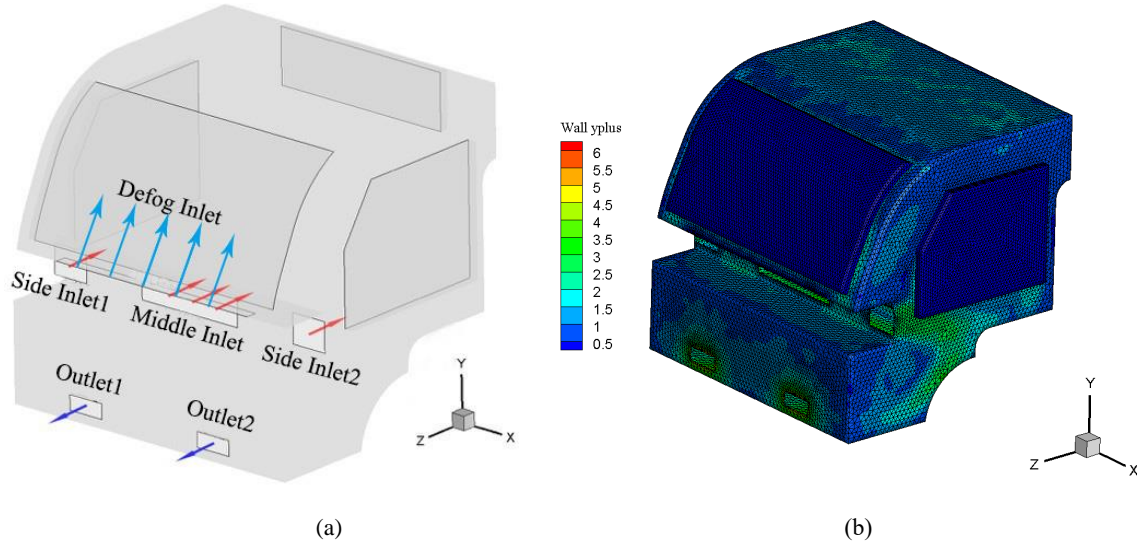


Figure 7: Computational domain of the internal flow field. (a) scheme of the inlets and outlets; (b) the distribution of y^+

Considering the complex shape of the model, unstructured tetrahedral mesh was used. To ensure better condensation effects, the window entity was retained. The y^+ value of the window is approximately 0.5 and the distribution is shown in figure 7(b), fully satisfying the mesh quality requirement.

3.3.3 Simulation conditions

To gain a better understanding of the system, various inlet flow conditions, i.e., the inlet type, the flow velocity, the relative humidity and the temperature, were tested. This resulted in a total of 36 test cases shown in table 5. The transient simulation method was adopted, where most settings were kept the same as in the validation test. The initial temperature in the cabin was unified and set at 288K. The averaged heat transfer coefficient obtained in Section 3.2 section was used as the input condition. The initial thickness of water film was set to 0.01mm to ensure that the cabin had certain humidity to achieve a faster condensation process.

Table 5: Inlet conditions for all the test cases in the present study.

Cases	Inlet Parameters				
	Velocity [m/s]	Temperature [K]	RH[%]	ω_{vap}	Inlet Types
(1) V1-T320-H100-1	0.1	320	100	0.0679	Middle
(2) V1-T320-H100-3	0.1	320	100	0.0679	Middle-Side
(3) V2-T320-H100-4	0.2	320	100	0.0679	Defog

(4)	V4-T320-H100-4	0.4	320	100	0.0679	Defog
(5)	V6-T320-H100-4	0.6	320	100	0.0679	Defog
(5)	V8-T320-H100-4	0.8	320	100	0.0679	Defog
(7)	V10-T320-H100-4	1	320	100	0.0679	Defog
(8)	V1-T330-H100-3	0.1	330	100	0.1173	Middle-Side
(9)	V1-T330-H80-3	0.1	330	80	0.0961	Middle-Side
(10)	V1-T330-H60-3	0.1	330	60	0.0739	Middle-Side
(11)	V1-T330-H40-3	0.1	330	40	0.0532	Middle-Side
(12)	V1-T330-H20-3	0.1	330	20	0.0259	Middle-Side
(13)	V1-T320-H100-3	0.1	320	100	0.0679	Middle-Side
(14)	V1-T320-H80-3	0.1	320	80	0.0551	Middle-Side
(15)	V1-T320-H60-3	0.1	320	60	0.0419	Middle-Side
(16)	V1-T320-H40-3	0.1	320	40	0.0291	Middle-Side
(17)	V1-T320-H20-3	0.1	320	20	0.0144	Middle-Side
(18)	V1-T310-H100-3	0.1	310	100	0.0409	Middle-Side
(19)	V1-T310-H80-3	0.1	310	80	0.0330	Middle-Side
(20)	V1-T310-H60-3	0.1	310	60	0.0249	Middle-Side
(21)	V1-T310-H40-3	0.1	310	40	0.0167	Middle-Side
(22)	V1-T310-H20-3	0.1	310	20	0.0085	Middle-Side
(23)	V1-T300-H100-3	0.1	300	100	0.0222	Middle-Side
(24)	V1-T300-H80-3	0.1	300	80	0.0179	Middle-Side
(25)	V1-T300-H60-3	0.1	300	60	0.0135	Middle-Side
(26)	V1-T300-H40-3	0.1	300	40	0.0090	Middle-Side
(27)	V1-T300-H20-3	0.1	300	20	0.0045	Middle-Side
(28)	V0.5-T320-H20	0.05	320	20	0.0144	Middle-Side
(29)	V1.5-T320-H20	0.15	320	20	0.0144	Middle-Side
(30)	V2-T320-H20	0.2	320	20	0.0144	Middle-Side
(31)	V0.5-T320-H60	0.05	320	60	0.0419	Middle-Side
(32)	V1.5-T320-H60	0.15	320	60	0.0419	Middle-Side
(33)	V2-T320-H60	0.2	320	60	0.0419	Middle-Side

(34) V0.5-T320-H100	0.05	320	100	0.0679	Middle-Side
(35) V1.5-T320-H100	0.15	320	100	0.0679	Middle-Side
(36) V2-T320-H100	0.2	320	100	0.0679	Middle-Side

V-velocity T-temperature H-relative humidity and the last number represents the number of inlets

3.3.4 Condensation at different positions of the cabin windows

It has been known that the dewing liquid film thickness on different windows are noticeably different. Figure 8 shows the variation of the averaged film thickness with the relative humidity (RH) for the cabin windows with fixed inlet flow temperature values of $T = 310\text{K}$ and 320K (cases 13-22). As can be seen, the variations of the liquid film thickness with RH are very similar in the two fixed temperature cases. It should be noted that the film thickness tends to increase with the inlet flow temperature.

Figure 9 presents the variation of the averaged film thickness with the inlet flow temperature at two fixed relative humidity values of $\text{RH} = 60\%$ and 20% . For $\text{RH} = 60\%$, the film thickness increases linearly with the inlet flow temperature in all the window cases. The front window exhibits the greatest film thickness and the fastest increasing rate. For $\text{RH} = 20\%$, the film thickness of all the window cases increases marginally for $T < 320\text{K}$, prior to a rapid increasing trend; however, the overall film thickness is relatively thin (close to the initial thickness of 0.01mm), indicating that low humidity results in slow condensation.

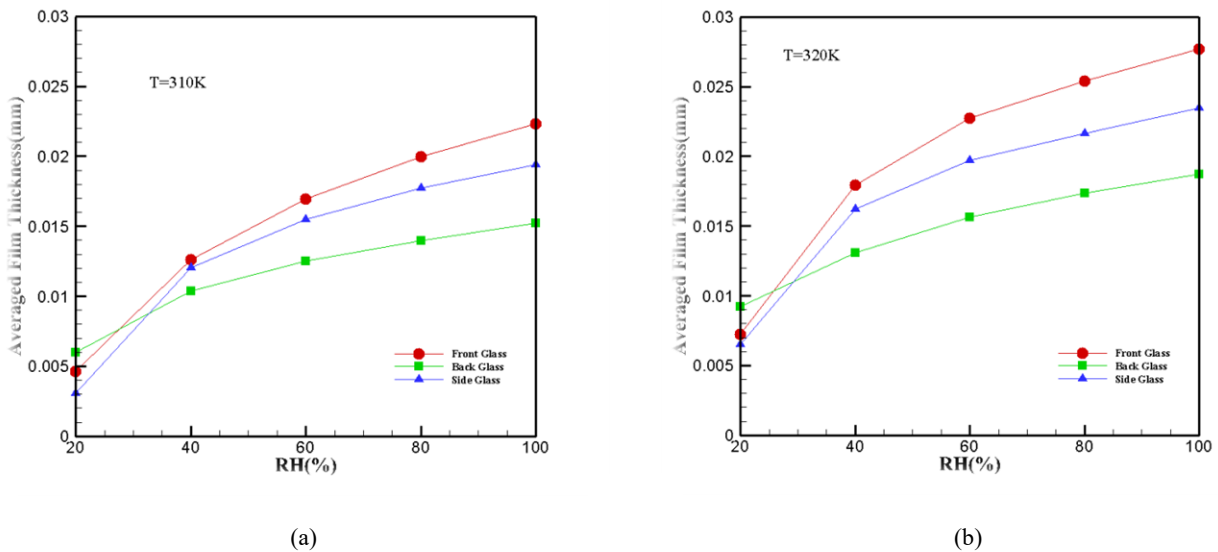


Figure 8. Variation of the liquid film thickness with the relative humidity at (a) $T=310\text{K}$ (b) $T=320\text{K}$.

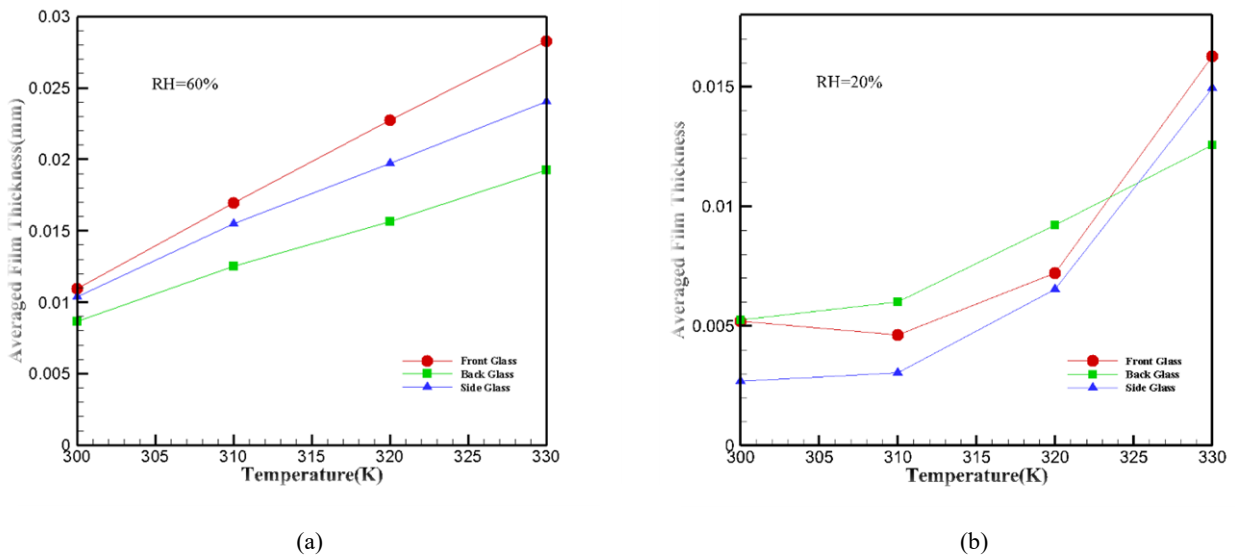


Figure 9. Variation of the liquid film thickness with the inlet flow temperature at (a) RH=60% and (b) RH=20%.

Furthermore, one representative case with $T = 320\text{K}$ and $\text{RH} = 60\%$ (case 15) was selected to demonstrate the evolution of the dewing process. Figure 10 shows the film thickness contours at four different time instances, $t = 100\text{s}$, 300s , 700s and 1000s . It can be seen that the condensation of the front and side windows starts from the top, while the rear window begins to dew from the bottom. At $t = 1000\text{s}$ when the condensation becomes saturated, the highest value appears at the lower part of the front window. It should also be noted that the condensation of the windshield window in general appears to be more severe than the side and rear windows. One primary factor for this seems to be the distance from the air-conditioning inlet. The results indicate that the front window can be used as an important object for analyzing the influence of the temperature and humidity on the condensation.

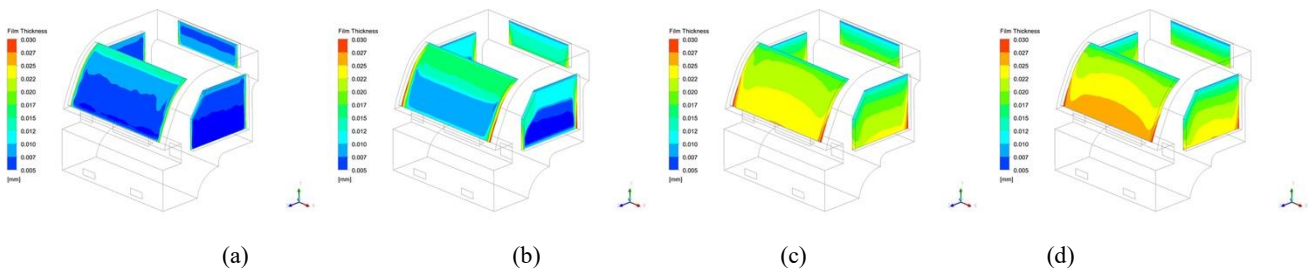


Figure 10: Evolution of the film thickness contours in the vehicle cabin at (a)100s (b)300s (c)700s (d)1000s

3.3.5 Influence of the temperature and humidity

The temperature and humidity are two main factors in the analysis of condensation mechanism in this study. Figure 11(a - c) shows the variations of the film thickness with RH for different fixed temperature values at $t = 1000s$, while figure 11(d) shows the variation of the mass of condensate water correspondingly. Clearly, these plots all show that increases in the temperature and humidity lead to aggravations in condensation. In other words, the effect of moisture on condensation gradually reduces as the relative humidity is increased. On the other hand, in general, increasing the temperature on condensation is of more significance.

Figure 12 presents the time evolution of the film thickness of the front window with a fixed temperature of 320K and different RH values. Clearly, the higher the relative humidity is, the higher the thickness of the liquid film and the faster the condensation rate will be, and the stability will be achieved earlier. Moreover, figure 13 plots the averaged temperature inside the cabin as a function of RH. As can be seen, the averaged temperature in the cabin decreases marginally as RH is increased. But when the inlet temperature is lower close to the cabin temperature, the influence of RH on the temperature in the cabin is not obvious any more.

To further evaluate the driver's thermal comfort, figures 14 shows the flow velocity contours in the center plane with five different RH values at fixed inlet temperature 320K, together with the resulted temperature contours in the $\frac{1}{4}$ plane (corresponding to the driver's position). As can be seen, increasing RH sees a stronger and larger flow field forming on the windshield window. This is most likely due to the increase in the water vapor mass fraction and the decrease in the air density making the air flow to roll up easier.

From the temperature contours, when RH is below 20%, the areas close to the driver's head and leg can achieve an excellent warmth effect, where the temperature is approximately 297K. As the humidity is increased, the high-temperature region shrinks gradually, and tends to shift from the driver's head position towards the front window. In the extreme cases with $RH = 20\%$, the high-temperature region is reduced to a small area around the upper part of the front window, implying that the upper body of the driver is not warmed effectively, while the temperature around the position of the driver's legs is even lower than the initial temperature (288K). From the above results, it can be concluded that increasing relative humidity can cause the internal airflows to roll up faster towards the front window and thus the warm-temperature region moves towards the upper part

of the cabin, which is not effective for the occupants' thermal comfort. Thus, it is suggested that the relative humidity is an important factor to be considered in the vehicle air-conditioning design.

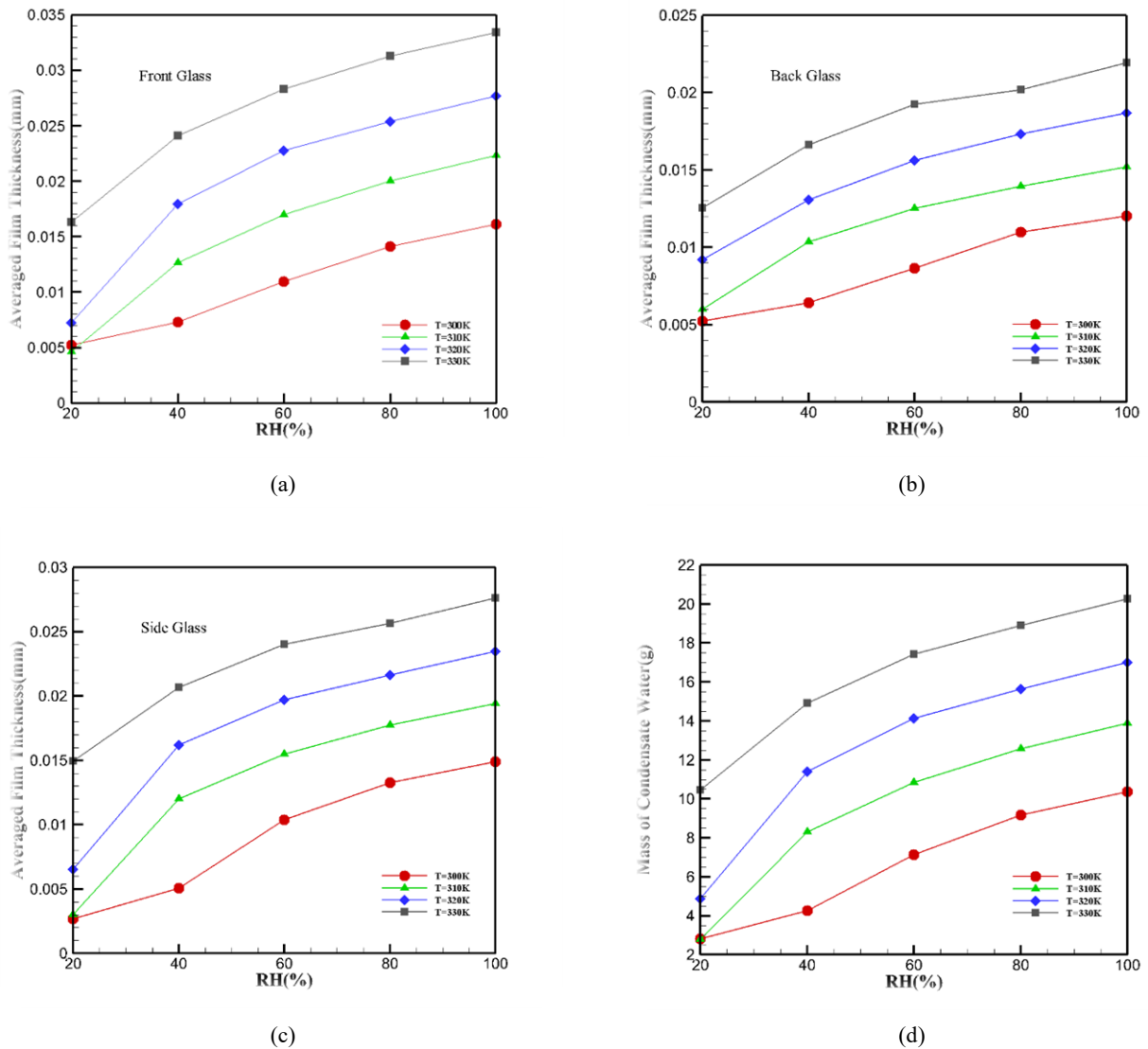


Figure.11 The Averaged liquid film thickness of (a) front glass (b) back glass (c) side glass and (d) the mass of condensate water in 1000s of cases with different RH and temperatures.

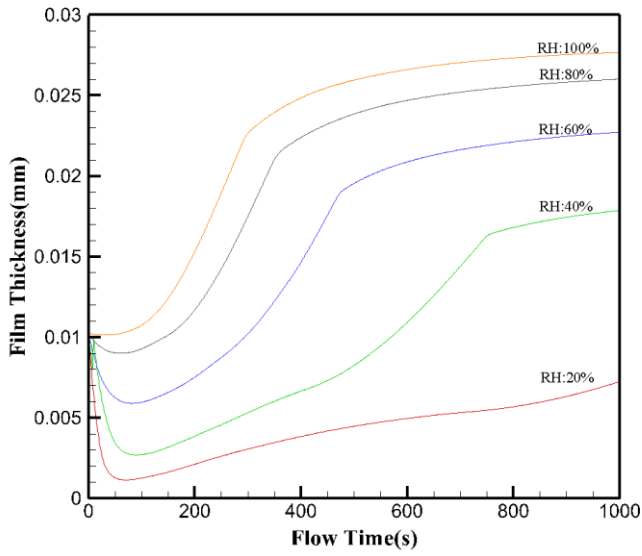


Figure.12 The Change of Liquid Film Thickness with Time at Different Relative Humidity

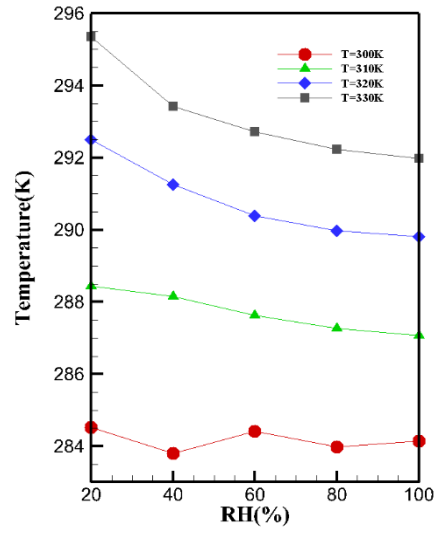
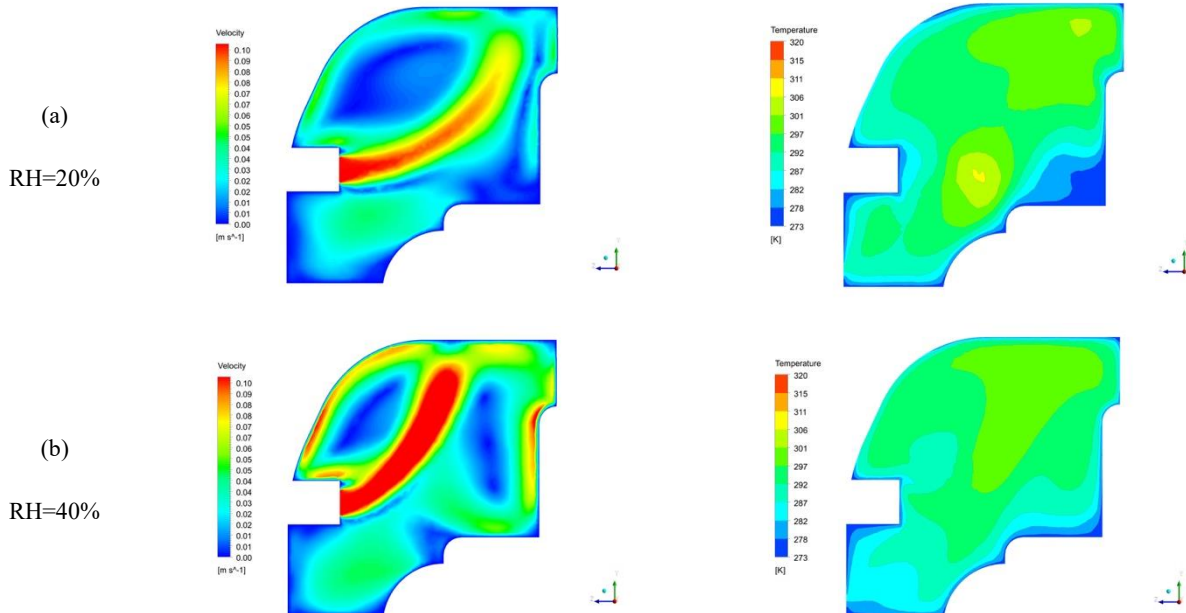


Figure.13 The relationship between the temperature of the cabin and the temperature and humidity of the inlet



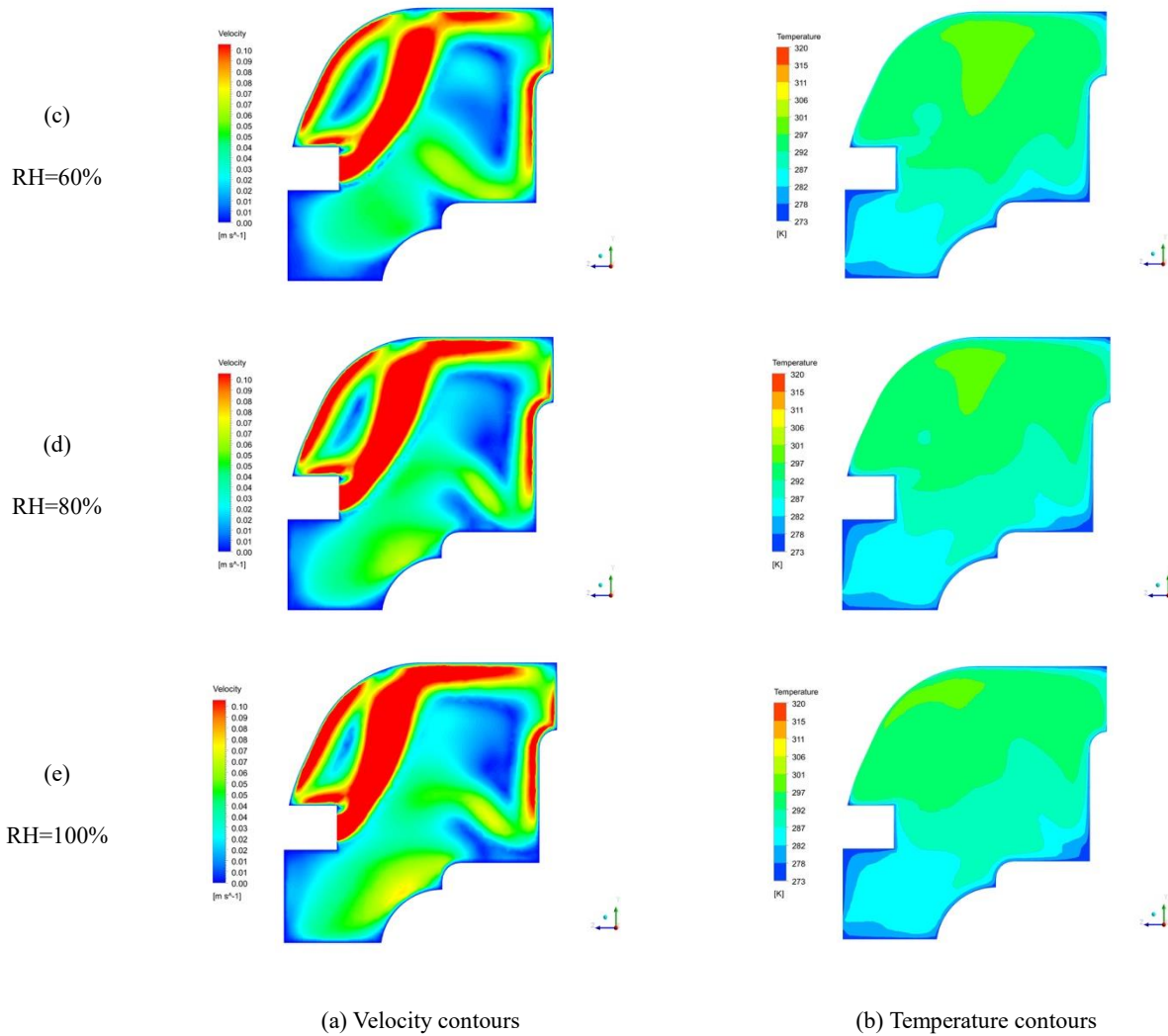


Figure 14: The interior flow contours in the center plane and the temperature contours in the $\frac{1}{4}$ plane for different RH values. The defogging airflow temperature is fixed at 320K, and the RH= (a) 20% (b) 40% (c) 60% (d) 80% (e) 100%

3.3.6 Influence of the inlet velocity

The distribution of condensation and temperature and humidity under four different inlet velocity is analyzed in this section. Figure 15 is the change of front window's film thickness with time of cases with different inlet velocity in 320K and RH60%. The basic trend of four curves is almost the same, while the final thickness increases with the rising of velocity. In the case of 0.05m/s, the final thickness is obviously lower than other conditions and fluctuation occurs in cases of 0.05m/s and 0.2m/s. Figure 16 shows the relationship between final film thickness and velocity in different RH conditions. In RH 60% and 100%, there is a positive relation between the thickness of the film and the velocity. In cases of RH 20%, there is no obvious difference of thickness at different velocity and it has a slightly decreasing trend with the increase of inlet velocity.

Figure 17 displays the contours of film thickness in different inlet velocity. At the velocity of 0.05m/s, the highest thickness of the front window film is located in the middle of the lower part and the thickness of the liquid film on both sides is obviously lower. With the increase of wind speed, the thickness of liquid film is distributed even more evenly in the horizontal direction and the two sides are also in the area with the highest thickness of the liquid film. Under the high velocity of 0.2m/s, the distribution of the film thickness is asymmetrical.

Figure 18 shows the streamline diagram in the vehicle cabin at different velocities. At the velocity of 0.05m/s, the air flows from the vent only a small distance and then flows upward, so the area near front window is strongly warmed and thus leads to the relatively lower film thickness. In cases with velocity of 0.1m/s and 0.15m/s, the flow field is relatively stable, while in cases of 0.05m/s and 0.2m/s, the flow is rather disorder and results in the fluctuation of curves in Figure.15.

Considering the heating effect, the diver's position is far below comfort temperature in cases of 0.05m/s, while the temperature in cases of 0.1m/s and 0.15m/s is more suitable and the temperature around area of the driver's head is about 295K. The temperature is excessive in cases of 0.2m/s which is over 300K that beyond the comfort temperature.

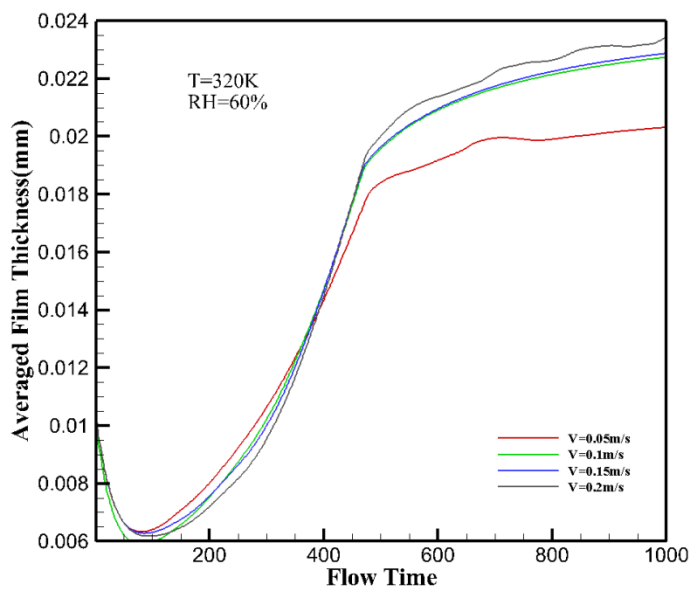


Figure.15 Change of film thickness with time under different inlet velocities

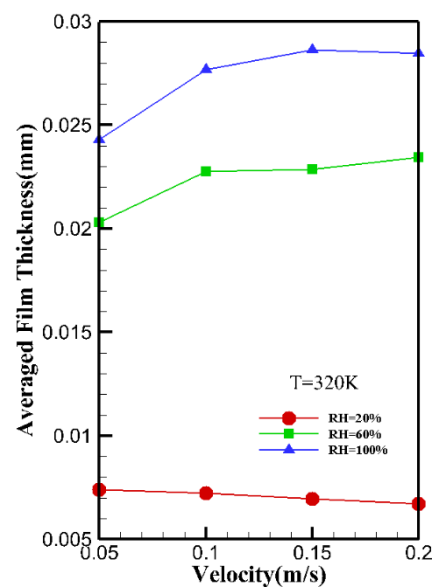


Figure.16 The relationship between the film thickness and the velocity

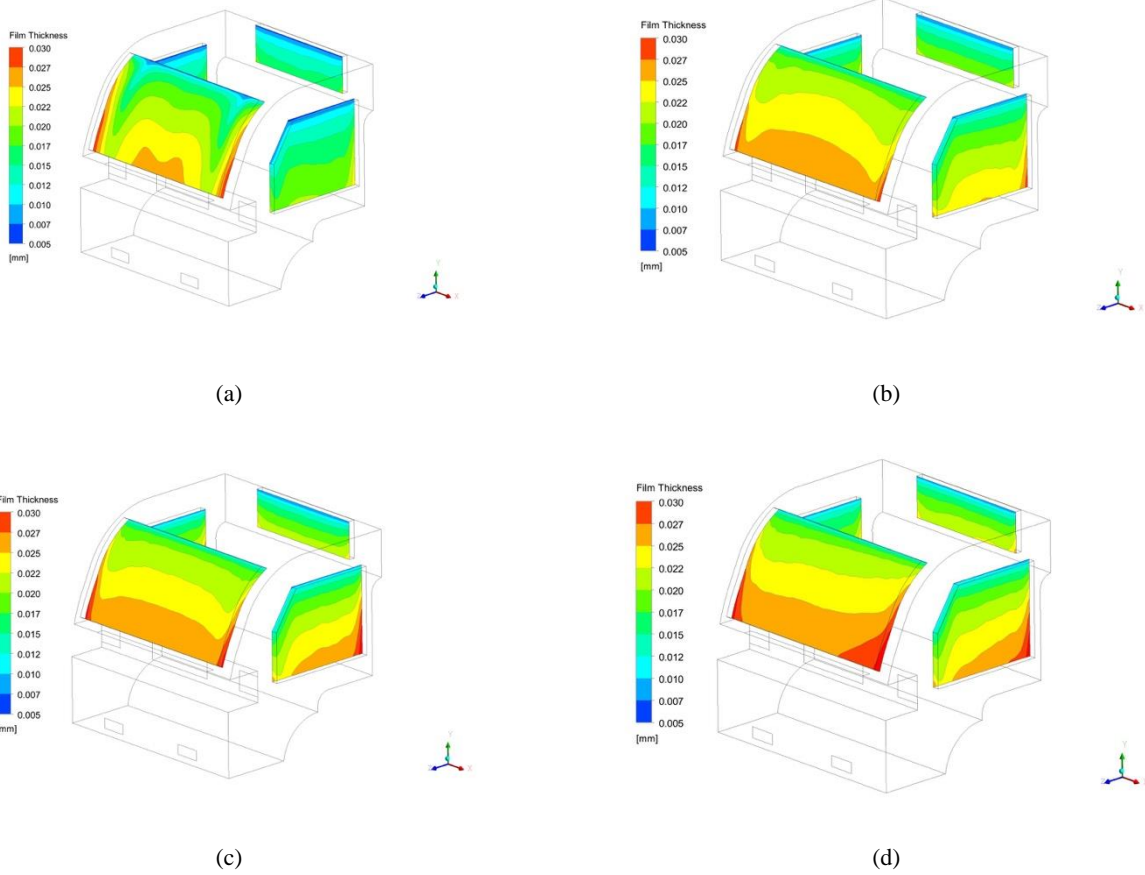
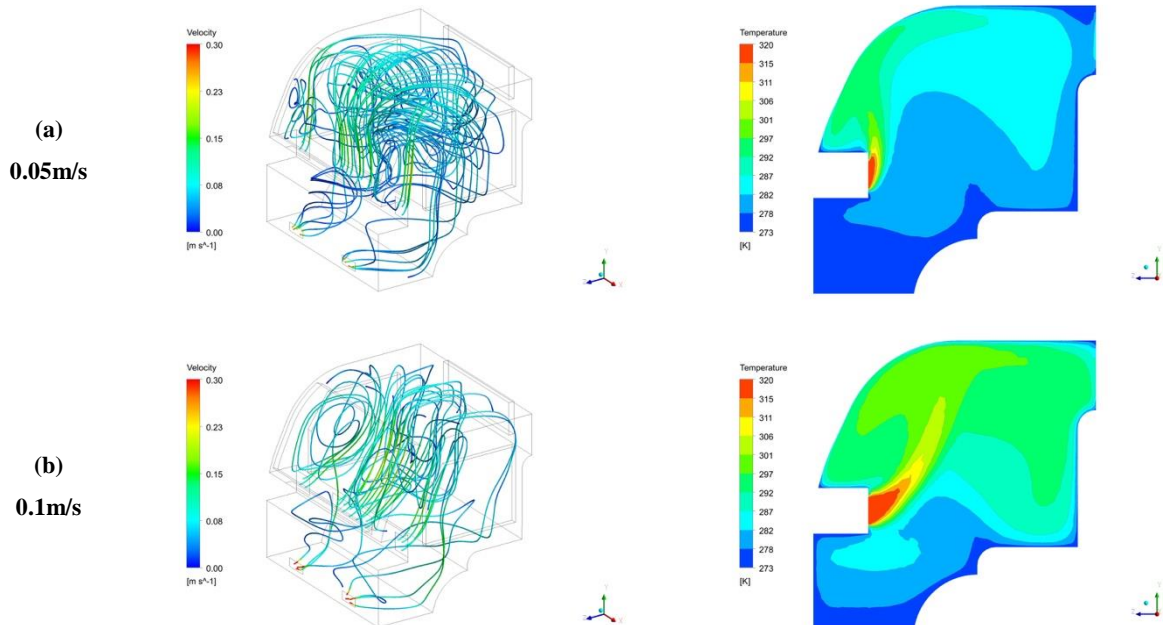


Figure 17: Contours of the dewing liquid film thickness when inlet flow velocities is (a) 0.05m/s (b) 0.1m/s (c) 0.15m/s (d) 0.2m/s



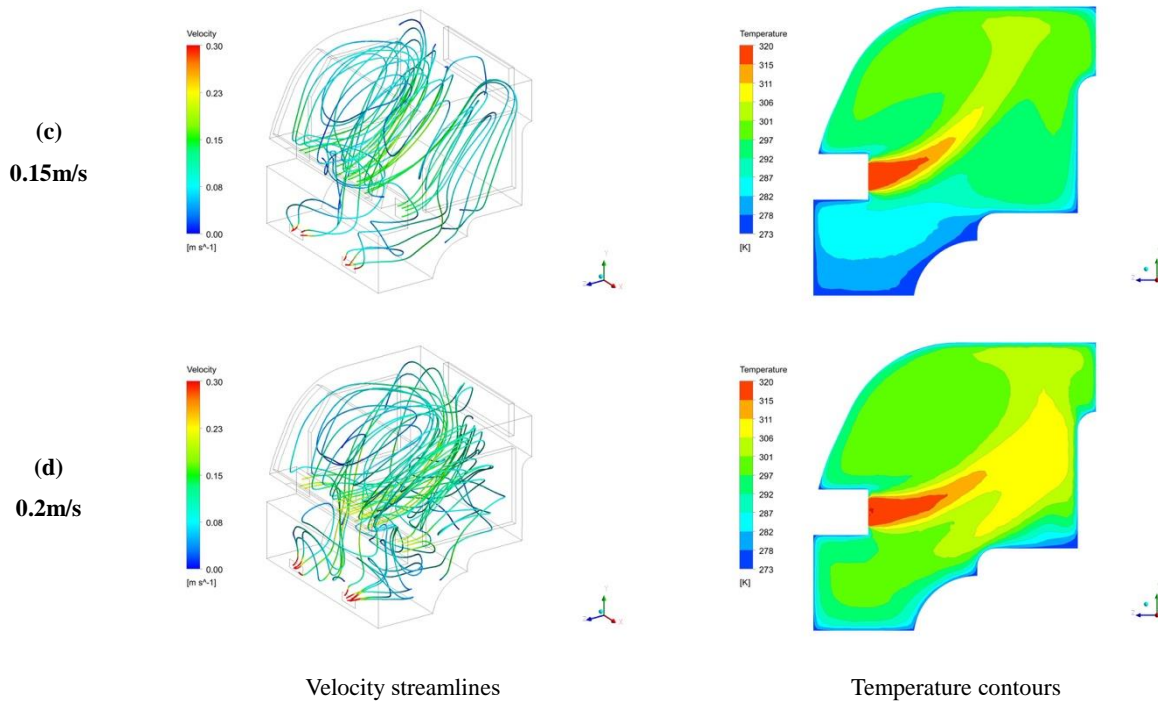


Figure 18: The interior flow velocity streamlines and temperature contours in the centerplane when the inlet velocity is (a) 0.05m/s (b) 0.1m/s (c) 0.15m/s (d) 0.2m/s.

3.3.7 Influence of the Defog Flow and Parameters

On the base of the case in last section, the defogging inlet which is located below the front window was opened at 2000s and different inlet velocities were simulated. The mass fraction of air from defog inlet was set to 0 and the temperature is 320K with 5 different velocities shown in table 5 (cases 3-7). The change of film thickness of each window with time under different velocities is shown in Figure 19. Figure 19(a-c) plot the change of film thickness for three different windows, while figure 19(d) evaluates the reduction percentage of the water film.

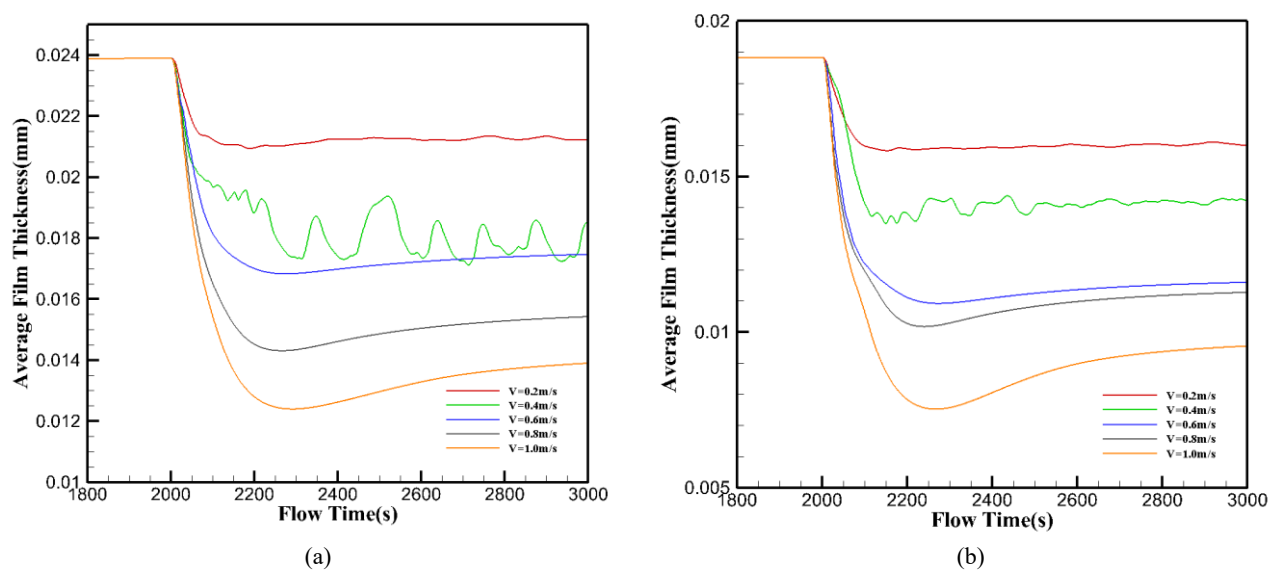
It could be noticed from these four pictures that the opening of defogging inlet could remove the dew on windows effectively. The best defogging effect is achieved when defogging is operated for approximately 200s when the water film was reduced to lowest. Keeping the defogging inlet open for too long may increase the film thickness on the back and side windows, rather than reducing the thickness of the film. Figure 20 shows the contours of film thickness at $t = 100s$ with different inlet velocities. The effect of inlet velocity on defogging is obvious. With the increase of velocity, the thickness drop and defogging speed is significantly strengthened.

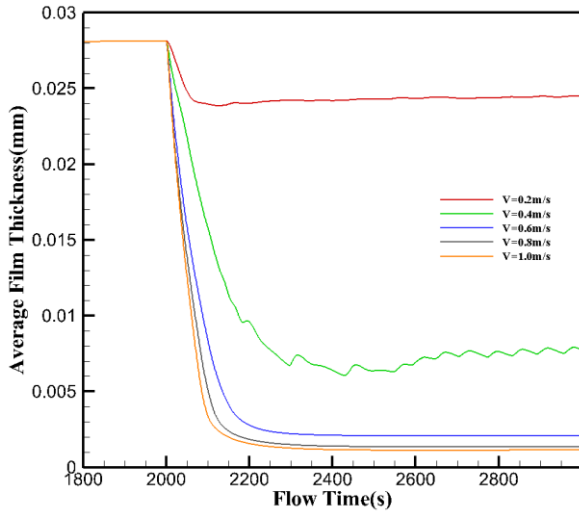
As indicated in figure 19(d), the defogging effect is mostly obvious for the front window, while much less effects are seen on the side window and back windows. The fog removal rate increases

rapidly with the increase of the velocity of inlet. However, when the velocity reaches a certain speed, the fog removal rate becomes limited. When the velocity of the defog inlet reaches 0.6m/s, the defogging effect of the front window is basically the highest and the film thickness will not decrease further with the increase of the velocity.

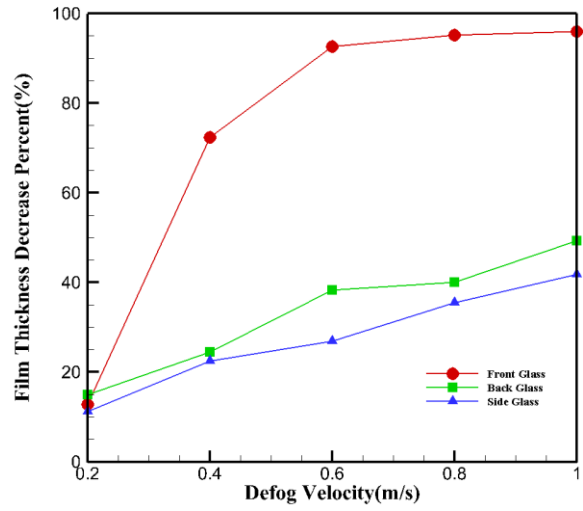
Figure 20 shows the velocity streamlines inside the cabin with different inlet velocities. For the velocity at 0.2m/s, the airflow from the inlet rises and then begins to fall back such that it cannot cover the front window surface at all. While in cases at 0.4m/s, where the film thickness fluctuates largely, the airflow first rises to the middle of front window and then starts to fall and intertwines with airflow from other inlet, and the whole flow field is quite disorder. This could be the main reason that leads to the fluctuation of film thickness. When the airflow velocity $\geq 0.6\text{m/s}$, the air can flow steadily through the whole front window and form a large stable eddy current in the cabin. In this case, the flow field in the cabin is more stable.

In conclusion, the defog inlet has a significant effect on diminishing dew on the front window. It was found that the optimum defogging airflow velocity is 0.6m/s, with which the most effective defogging is achieved with significant energy saving. It was also found that the effective defogging effect could be reached after opening the inlet for 100s; however, longer operation time may result in adverse effects to cause increases in the film thickness, and also cause overheating that adversely affects driving comfort in the cabin.



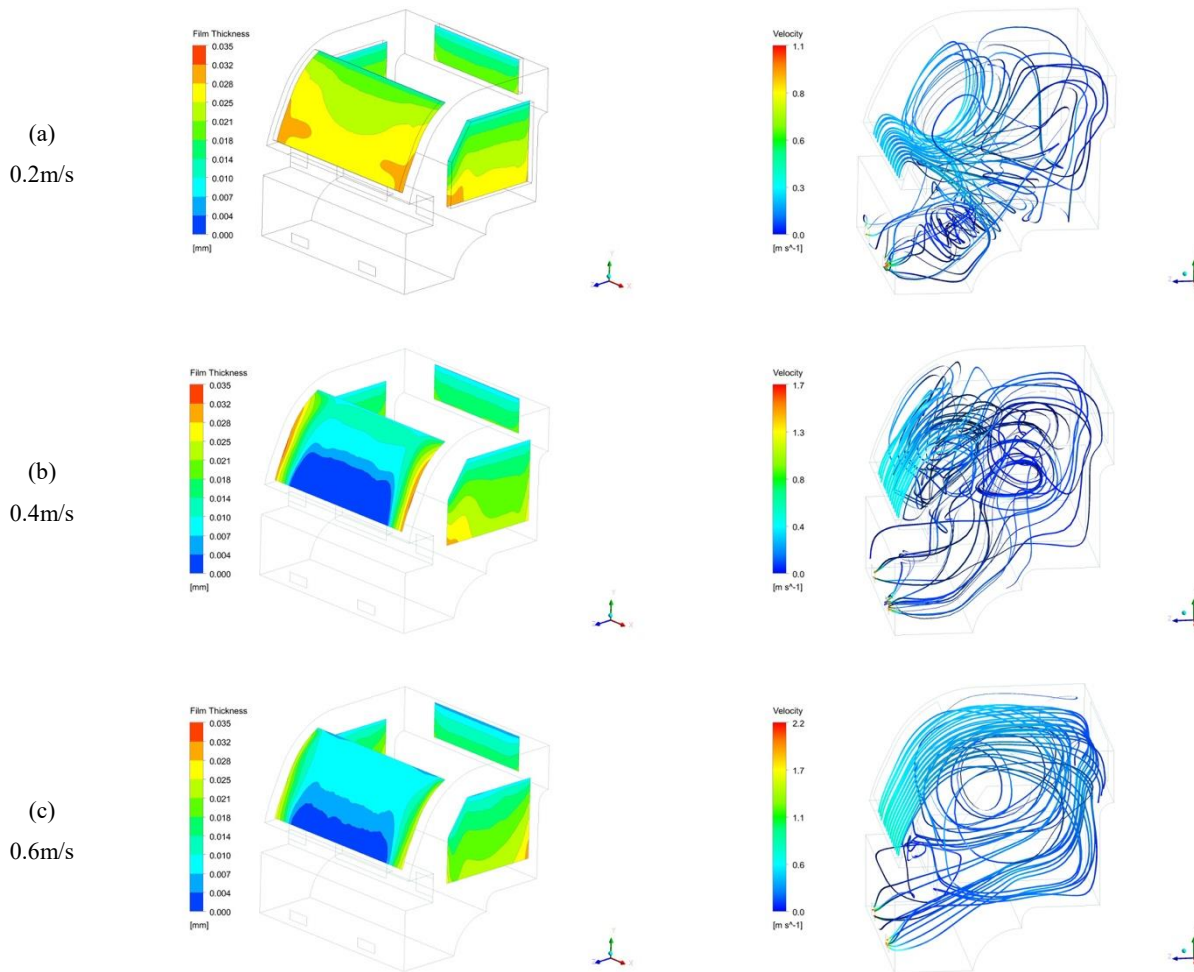


(c)



(d)

Figure.19 The change of film thickness with time under different defog velocities at (a) front glass (b) back glass (c) side glass, and (d) the drop percentage of film under different defog velocities



(a)
0.2m/s

(b)
0.4m/s

(c)
0.6m/s

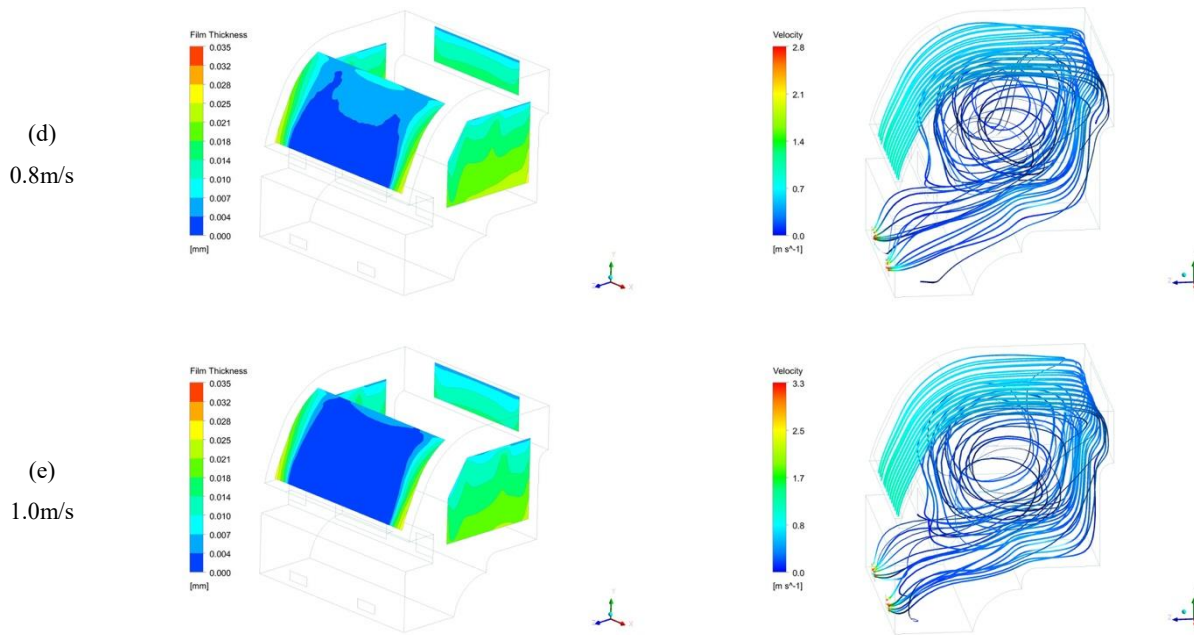


Figure.20 The film contours and velocity streamlines in 100s when defog velocity at (a) 0.2m/s (b) 0.4m/s (c) 0.6m/s (d) 0.8m/s and (e) 1.0m/s

3.4 An overall evaluation

In this section, an overall assessment of all cases tested in this study, by considering the condensation, the thermal comfort standard of temperature and humidity in the cabin, and the economic efficiency synthetically.

Figure 21 presents the distribution of all the test cases in the plane of the temperature and relative humidity. As highlighted in red, four cases (12, 17, 29 and 30 in table 5) fall in the comfort zone ($30\% < RH < 60\%$ and $292K < T < 298K$) at 1000s. Which would be useful to provide references for the future design of vehicular air conditioning systems.

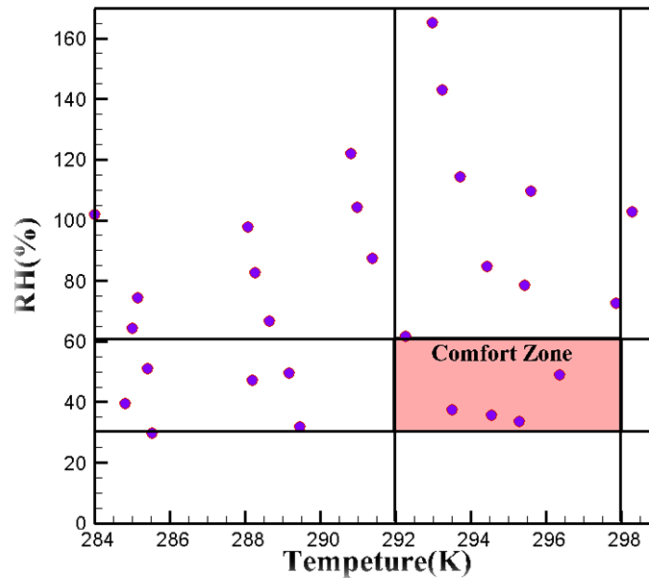


Figure 21: Distribution of the cabin temperature and RH for all the test cases at 1000s.

4. Conclusions

This paper has numerically studied the dewing phenomenon and defogging progress of a truck cabin model. By comparing with previous experimental results of CONAN model, the EWF model of ANSYS FLUENT combined with UDF was validated to be successfully in simulating the dewing problem. Then the study was focused on the dewing phenomenon of a truck cabin, where the heat dissipation of window glasses was considered by simulating the external flow field. A total of 33 different working conditions with different temperature and relative humidity of air-condition system flow velocities were simulated to better understand the development of dewing film. The defogging airflow was also discussed with different flow velocities to evaluate the defogging performance.

It was found through the external flow velocity field, the convective heat transfer coefficient of the front window was higher than that of the side and back windows. This is most likely due to the differences in the external flow velocity around different parts of the cabin surfaces.

The temperature and humidity in the cabin are two important factors in the condensation process of the windows. The present results showed that reducing the humidity could not only effectively control the condensation, but also optimize the distribution of the internal airflow and increase the heating effect. On the other hand, low cabin temperature affects the occupants' thermal comfort, whereas high temperature will increase the content of water vapor in the cabin, thereby

worsening the problem of condensation.

The defogging airflow velocity was found to have a significant impact on the liquid film thickness. When the defogging airflow velocity was greater than 0.6m/s, the dew on the front window was diminished rapidly. In addition, the operation time of the demister should be approximately 200s to achieve desired defogging effects; otherwise, longer operation time may result in not only inefficient energy consumption but also excessive temperature rise adversely affecting the occupants' comfort in the cabin.

To satisfy the comfortable (proper temperature), efficiency (lower velocity with lower fan energy consumption), and safety (thin film) requirements in the same time, this paper suggests that the automobile air conditioner could be controlled within the relative humidity range of $20\% < RH < 60\%$ and the temperature range of $292K < T < 298K$.

Acknowledgement

The authors gratefully acknowledge the financial support from the National Natural Science Foundation of China grant No. 91741203.

References

- [1]. E.M, Sterling, E. M. Criteria for human exposure to humidity in occupied building, *Ashrae Transactions B*, 91(Pt 1):611-622.
- [2]. A. Palmowska, B. L. Experimental study and numerical prediction of thermal and humidity conditions in the ventilated ice rink arena, *Building and Environment*, 108:171-182.
- [3]. J. Hara. Study on the Refrigeration Cycle of Automotive Air Conditioners, *Symposium on Man-Thermal Environment System ICHES*, 91:195-198.
- [4]. A. Dehbia, F. J., B. Prediction of Steam Condensation in the Presence of Noncondensable Gases Using a CFD-based Approach, *Nuclear Engineering and Design*, 258:199–210.
- [5]. G. Zschaeca, T. F., A.D. Burns. CFD Modelling and Validation of Wall Condensation in the Presence of Non-condensable Gases, *Nuclear Engineering and Design*, 279:137-146.
- [6]. P. Birbarah, N. M. Internal Convective Jumping-droplet Condensation in Tubes, *International Journal of Heat and Mass Transfer*, 114:1025–1036.

-
- [7]. U. Kleinhan, R. R. c., S. Schmid. Alkali Vapor Condensation on Heat Exchanging Surfaces: Laboratory-Scale Experiments and a Mechanistic CFD Modeling Approach, *Energy & fuels*, 30:9793-9800
- [8]. J. Liu, H. A., H. Yoshino. CFD Prediction of Surface Condensation on Walls and its Experimental Validation, *Building and Environment*, 39:905–911.
- [9]. T. Sriveerakul, S. A., K. Chunnanond. Performance Prediction of Steam Ejector Using Computational Fluid Dynamics: Part 1. Validation of the CFD results, *International Journal of Thermal Sciences*, 46:812–822.
- [10]. P. F. He, B. Z., C. Zhu, et al. Dynamic Process Modeling on Depressurization by Cooling-controlled Condensation in a Closed Chamber, *International Journal of Heat and Mass Transfer*, 78:330–340.
- [11]. J Hara, K. F, K. Kuwahara. Computer Simulation of Passenger Compartment Airflow, SAE Paper 881749.
- [12]. S. J. You, W. Q. L., T. Z. Ye, et al. Study on Moisture Condensation on the Interior Surface of Buildings in High Humidity Climate, *Building and Environment*, 125:39-48.
- [13]. J.W. Wan, J. V. d. K. Influence of the Position of Supply and Exhaust Openings on Comfort in a Passenger Vehicle, *International Journal of Vehicle Design*, 12:588-597.
- [14]. J. Curre. Numerical Simulation of the Flow in a Passenger Compartment and Evaluation of the Thermal Comfort of the Occupants, SAE Paper 970529.
- [15]. B. S, AbdulNour. Numerical Simulation of Vehicle Defroster Flow Field, SAE Paper 980285.
- [16]. J. Karim, B. S. A., G. C. Wiklund. State of Knowledge and Current Challenges in Defrosting Automotive Windshields, SAE Paper 980293.
- [17]. A. Aroussi., A. H., B. Clayton. Improving Vehicle Windshield Defrosting and Demisting, SAE Paper 2000-01-1278.
- [18]. A. Aroussi, S. A. A. A. G., A. Hassan, et al. Assessing the Performance of Electrically Heat Windshield, SAE Paper 2002-01-0225.
- [19]. A. Aroussi, A. H., B. Clayton. Vehicle Side-window Defrosting and Demisting process, EACC 2003, 155-163.
- [20]. R. A. Dwiartono, C. W. S., B. A. Nour, et al. The Use of Numerical Simulation to Perform Engineering Calculation of Window Defogging, SAE Paper 2005-01-2054.
- [21]. R. B. Kharat, M. R. N. S. R. K. Modeling of In-Cabin Climate and Fogging of Windshield, SAE Paper 2007-01-0767.
- [22]. ANSYS Inc. ANSYS FLUENT 17.0 User Guide,

-
- [23]. DL. Zeng, Y. A., XM. Zhang. *Engineering Thermodynamics*. 3rd ed, Higher Education Press: Beijing, China, 2002.
- [24]. W. Ambrosini, M. B., N. Forgone1. Comparison and Analysis of the Condensation Benchmark Results, The 3rd European Review Meeting on Severe Accident Research (ERMSAR-2008) Nesseber, Vigo Hotel, Bulgaria, 23-25 September 2008.
- [25]. L. Vyskocil, J. S., J. Macek. CFD Simulation of Air-steam Flow with Condensation, *Nuclear Engineering and Design*, 279:147-157.
- [26]. M. Y, Liang. Study on the Bending Performance of Toughened Glass Bearing Floor Under High Temperature, Master Thesis, Beijing University of Civil Engineering and Architecture, Beijing, 2017.
- [27]. Y. Yang, J. X. C., Y. Q. Huang. Analysis on the influence of gap flow around a tractor-trailer, 13th International Conference on Heat Transfer, Fluid Mechanics and Thermodynamics, 2017.
- [28]. J. Liu, H. Z., G. Zhang, X. Zhang, J. Tang, C. Tian. Experimental study and numerical simulation concerning fogging characteristics and improvement of return air utilization for electric vehicles, *Applied Thermal Engineering*, 129:1115-1123.